analytical chemistry

Article

pubs.acs.org/ac

Polypyrrole Nanotube Embedded Reduced Graphene Oxide Transducer for Field-Effect Transistor-Type H_2O_2 Biosensor

Jin Wook Park,[†] Seon Joo Park,[†] Oh Seok Kwon,[†,‡] Choonghyeon Lee,[†] and Jyongsik Jang*[,†]

[†]School of Chemical and Biological Engineering, Seoul National University, Seoul 151-742, Korea

[‡]Department of Chemistry, Massachusetts Institute of Technology, 77 Massachusetts Avenue, Cambridge, Massachusetts 02139, United States

Supporting Information

ABSTRACT: We report a rapid-response and high-sensitivity sensor with specificity toward H_2O_2 based on a liquid-ion-gated field-effect transistor (FET) using graphene-polypyrrole (PPy) nanotube (NT) composites as the conductive channel. The rGO, PPy, NTs, and nanocomposite materials were characterized using Raman spectroscopy, Fourier transform-infrared (FT-IR) spectroscopy, transmission electron microscopy (TEM), and scanning electron microscopy (SEM). On the basis of these results, a well-organized structure is successfully prepared owing to the specific interactions between the PPy NTs and the rGO sheet. Reliable electrical contacts were developed between the rGO/PPy NTs and the microelectrodes, which remained stable when exposed to the liquid-phase analyte. Liquid-ion-gated FETs composed of these graphene nanocomposites exhibited hole-transport behavior with conductivities higher than those of rGO sheets or PPy NTs. This implies an interaction between the PPy NTs and the rGO layers, which is explained in terms of the PPy NTs forming a bridge between the rGO layers. The FET sensor provided a rapid response in real time and high sensitivity toward H_2O_2 with a limit of detection of 100 pM. The FET-type biosensing geometry was also highly reproducible and stable in air. Furthermore, the liquid-gated FET-type sensor exhibited specificity toward H_2O_2 in a mixed solution containing compounds found in biological fluids.

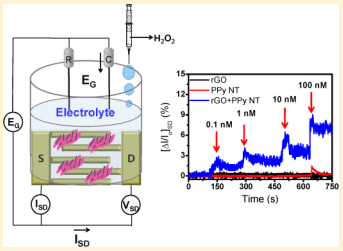

Detecting hydrogen peroxide (H_2O_2) is an important challenge for applications including healthcare, food science, pharmaceutical science, and environmental monitoring.[1] H_2O_2, a reactive oxygen species, has been linked to several bodily disorders such as atherosclerosis, cancer, and Alzheimer's disease.[2] In contrast, H_2O_2 is also a component in the physiological signaling pathways of healthy cells and is essential for cell growth, differentiation, migration, and immune system function.[3] Thus, an accurate and sensitive means of detecting H_2O_2 is important for clinical diagnostics and patient monitoring. Several methods of detecting H_2O_2 have been proposed, including various spectroscopic, electrochemical, colorimetric, and fluorescence-based methods.[4] Among these, electrochemical sensing of H_2O_2 has been most actively studied owing to its high sensitivity and specificity. Most electrochemical sensors are composed of enzymes or proteins, which bind to H_2O_2. However, natural enzymes often suffer from inefficiency, limited stability, and sensitivity to environmental factors. Recently, metal nanomaterials, including Ag, Au, Pt, and Pd nanoparticles, have been studied as alternative electrochemical catalysts to construct nonenzymatic hydrogen peroxide sensors.[5] However, growing concerns with regard to rare resources, such as noble metals, give rise to the development of low-cost, high-performance detection systems for H_2O_2 in practical applications.

Field-effect transistors (FETs) have attracted interest as primary candidates for fabricating state-of-the-art sensor platforms due to their ability to achieve high current amplification while maintaining a relatively high signal-to-noise ratio.[6] In particular, one-dimensional (1D) nanomaterials that exhibit high charge carrier mobility along the long-axis can be exploited for use in highly sensitive sensors.[7] Among various 1D nanomaterials, the remarkable physical and chemical characteristics of 1D conducting polymers (CPs) at the nanometer scale provide outstanding sensing performance in biosensor applications.[8] These 1D CP nanomaterials boast several advantages, including facile functionalization and biocompatibility. Recently, the possibility of fabricating biosensors using 1D liquid-ion-gated field-effect transistors (FETs) based on carboxylated-PPy nanomaterials has been reported.[9] However, a more rapid response and higher sensitivity are required for practical applications.

The emergence of graphene nanosheets has opened a new path for the utilization of 2D carbon materials as supports due to their high specific surface area, excellent electronic conductivity, and high chemical stability.[10] These remarkable features have attracted a great deal of attention in many fields, including nanomaterials, nanotechnology, electrical devices, and sensors.[11] Recently, H_2O_2 sensing devices based on graphene have been reported.[12] However, the sensitivity, selectivity, and response times of these sensors were relatively poor and insufficient for using in most practical applications. In order to

Received: November 20, 2013
Accepted: January 4, 2014
Published: January 4, 2014

   dx.doi.org/10.1021/ac403770x | *Anal. Chem.* 2014, 86, 1822−1828

Scheme 1. Schematic Illustration of the Synthesis of rGO/PPy NT Composites

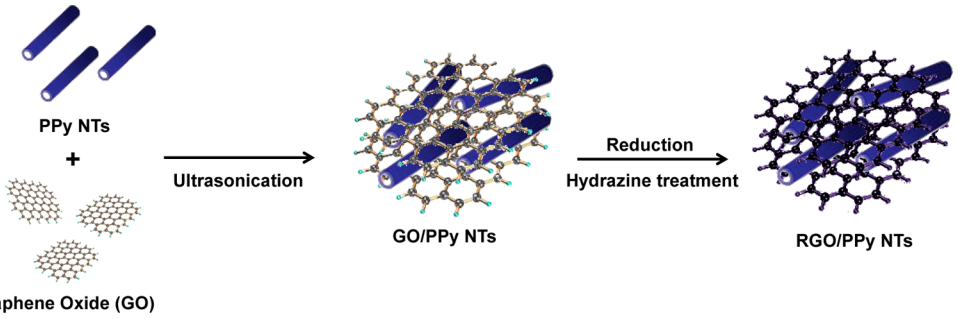

overcome these obstacles and enhance H_2O_2 detection, various metal and metal oxide nanomaterials, such as Ag, Au, Pt, ZnO, TiO_2, and Fe_3O_4, have been dispersed on the surface of the graphene sheet.[13] Unfortunately, these processes are expensive and require multiple steps for sample preparation. Therefore, the development of a new class of hybrid materials, created using simple and facile synthetic methods, is needed to create high-performance biosensors.

In this article, we demonstrate high-performance FET-type H_2O_2 sensors based on rGO transducers with embedded PPy NTs. The graphene-PPy NT hybrids described herein exhibited enhanced conductivity and surface area and yielded unprecedented sensing performance. The synthesis of these rGO/PPy NT composites involves only two main steps, as illustrated in Scheme 1. Graphene nanocomposites were formed by exploiting electrostatic interactions between negatively charged GO and positively charged PPy nanotubes (NTs). Even after hydrazine treatment to reduce the GO on the nanocomposites, the morphology and structure were not compromised due to the strong $\pi-\pi$ intermolecular interactions. PPy materials display p-type semiconductor behaviors. Unaltered graphene materials exhibit ambipolar properties in electrical devices. In this study, however, graphene showed hole-transporting behavior due to the absorption of oxygen and/or water from air,[14] resulting in rGO/PPy NT composites with enhanced p-channel FET behavior. The electrical behavior of these rGO/PPy NTs was also enhanced relative to that of PPy NTs and rGO layers due to enhanced conductivity, which resulted from PPy NTs acting as conductive channels between the rGO layers. The real-time response of liquid-ion-gated FET sensors based on rGO/PPy NT composites to H_2O_2 was particularly rapid (<1 s). The intensity of the response increased with increasing H_2O_2 concentration, and the detection limit was approximately 100 pM, which is about 1 order of magnitude lower than the lowest previously reported detection limit for an H_2O_2 sensor system. Furthermore, a high degree of specificity toward H_2O_2 was observed. To the best of our knowledge, this is the first example of a high-sensitivity FET-type sensor based on rGO/PPy NT composites.

EXPERIMENTAL SECTION

Materials. Pyrrole (98%), hydrogen peroxide (30%), uric acid (UA), ascorbic acid (AA), glucose, graphite flakes, methyl orange (MO), and ferric chloride ($FeCl_3$, 97%) were purchased from Aldrich Chemical Co. and used without further purification.

Synthesis of 1-D PPy nanomaterials. The preparation of PPy NTs was carried out using a self-degraded template method.[15] $FeCl_3$ (0.243 g, 1.5 mmol) was added to a 5-mM MO solution (sodium 4-[4′-(dimethylamino)phenyldiazo] phenylsulfonate, $(CH_3)2NC_6H_4-N{=}NC_6H_4SO_3Na$) in deionized water. After a flocculent precipitate appeared, the pyrrole monomer (105 μL, 1.5 mmol) was added, and the mixture was stirred at room temperature for 24 h. The resulting precipitate was purified by washing it with deionized water and methanol several times until the filtrate was colorless and had a neutral pH. The powdered PPy NTs (0.08 g, 79.5%) were then dried under vacuum at 60 °C for 24 h.

Synthesis of rGO/PPy Nanocomposites. GO was obtained from graphite powder using a modified Hummers and Offeman method.[16] GO was dispersed in water with a concentration of 0.06 mmol and then mixed with PPy NTs (also at a concentration of 0.06 mmol). The mixtures were ultrasonicated for 1 h. The resulting GO/PPy NT structures were exposed to 5 μL (35 wt %) of hydrazine solution for 1 h at 95 °C, which reduced GO to rGO. The final product, an rGO/PPy NT composite (0.055 mmol, 91.7%), was obtained via filtration, purified using water, and dried in a vacuum oven at 25 °C for hours.

Fabrication of rGO/PPy NT Composite FET Sensor. A microarray, consisting of 80 pairs of gold interdigitated microelectrodes, was patterned on a glass substrate using a 50-nm-thick Cr adhesion layer via a photolithographic process, resulting in electrodes with a gold layer thickness of 50 nm, a width of 10 μm, length of 4000 μm, and an interelectrode spacing of 10 μm. The microelectrode substrate was cleaned using sonication in ethanol. An aliquot of 0.1 mL of the ethanol solution containing 0.1 wt % rGO/PPy NT composites was dropped onto the interdigitated electrodes. The microelectrode substrate was finally dried under vacuum at room temperature for hours.

A solution chamber (volume 10 mL) was designed and employed for all solution-based measurements. The FET sensor substrate based on liquid-ion gate was fabricated with phosphate-buffered solution (PBS, pH 7.5). The current change of the sensor substrate was monitored at room temperature with a sourcemeter connected to a computer.

Instrumentation. The TEM images were taken with a JEOL JEM-2100 microscope. For TEM observation, the samples were diluted with ethanol and then the diluted solution was deposited on a copper grid coated with a carbon film. The FE-SEM images were obtained with a JEOL JSM-6700 F microscope. A specimen was coated with a thin layer of gold to eliminate charging effects. Raman spectra were recorded with a T64000 (Horiba Jobin Yvon). ATR-FTIR spectra were collected with a Thermo Scientific Nicolet 6700 FTIR spectrophotometer. X-ray diffraction (XRD) patterns were carried out with a New D8 Advance (Bruker). All electrical

dx.doi.org/10.1021/ac403770x | Anal. Chem. 2014, 86, 1822−1828

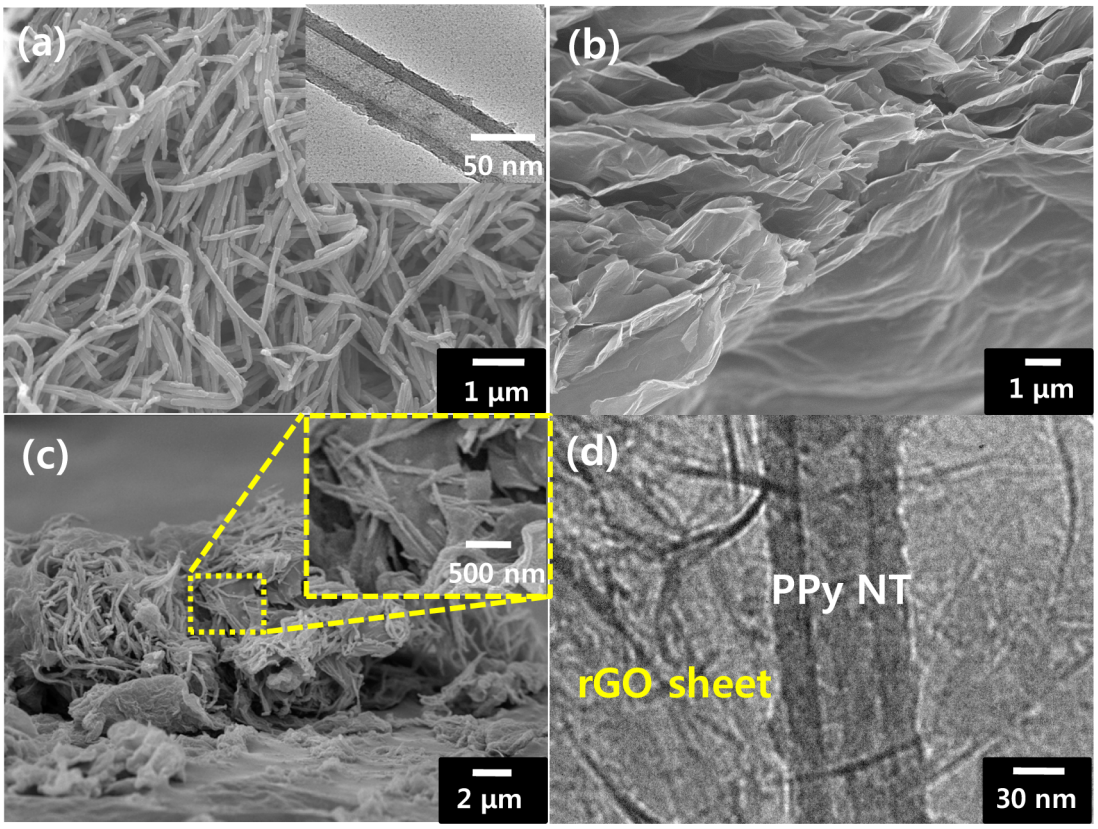

Figure 1. (a) SEM image shows PPy NTs. The inset shows a TEM image. Cross-sectional SEM images show (b) rGO and (c) rGO/PPy NTs. The inset indicates the magnification level. (d) A TEM image shows rGO/PPy NTs.

measurements were conducted with a Keithley 2612A sourcemeter, a probe station (MS TECH, model 4000) and a Wonatech WBCS 3000 potentiostat.

RESULTS AND DISCUSSION

The morphology of the rGO/PPy composites was characterized using scanning electron microscopy (SEM) and transmission electron microscopy (TEM). Figure 1a shows the SEM and TEM images of the PPy NTs, revealing that the diameter of the tubes was in the range of 70−80 nm. Figure 1b shows a cross-sectional SEM image of the rGO sheet, which exhibits a structure that resembles paper with porous spaces. Figure 1c,d shows cross-sectional SEM and TEM images of the rGO/PPy NT composite material. The structure of the PPy NT composites was well organized on the large surface area of the rGO sheets. Note that the PPy NTs interact with the rGO sheets. These interactions are discussed in detail below. These results indicate that the rGO/PPy NT composites were stable, which is attributed to the strong $\pi-\pi$ interactions between the rGO layers and PPy NTs.

To gain insight into the structure of the rGO/PPy NT composites, Raman spectroscopy was carried out and the resulting spectra are shown in Figure 2. The Raman spectrum of GO showed D peaks at 1364 cm^{-1} and G peaks at 1610 cm^{-1}. The Raman spectrum of the rGO exhibited two prominent bands at 1343 cm^{-1} and 1592 cm^{-1}, which correspond to D and G bands. The Raman spectrum of PPy NTs showed the C═C backbone stretching at ∼1577 cm^{-1} and the ring stretching mode of PPy at 1361 cm^{-1}. The Raman spectrum of the rGO/PPy NT composites exhibited an

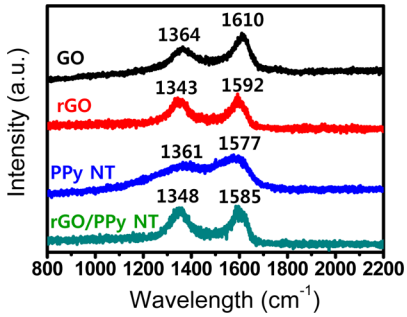

Figure 2. Raman spectra of GO, rGO, PPy, NT, and rGO/PPy NT composites.

increased intensity of the band around 1348 cm^{-1}, which indicates an interaction between PPy and the rGO sheets.

We measured attenuated total reflectance (ATR)-Fourier transform-infrared (FT-IR) and X-ray diffraction (XRD) spectra, as shown in Figure 3. GO exhibited characteristic absorption bands of oxide groups, including the C═O stretching peak at 1733 cm^{-1}, the vibration and deformation peaks of O−H groups at 3391 cm^{-1} and 1417 cm^{-1}, and the C−O (alkoyl) stretching peak at 1037 cm^{-1}. Most of the peaks related to oxygen-containing functional groups vanished in the FT-IR spectra of rGO, which means that the reduction of GO was successful. The characteristic bands of the rGO/PPy NT composites showed the pyrrole ring and graphene fundamental vibrations, which occur at 1561 cm^{-1} (C═C stretching), 1437 cm^{-1} (C−C stretching), 1282 cm^{-1} (C−N stretching), and 1038 cm^{-1} (C−H deformation). The peaks of the rGO/PPy NT composites were shifted compared with those of the PPy

dx.doi.org/10.1021/ac403770x | Anal. Chem. 2014, 86, 1822−1828

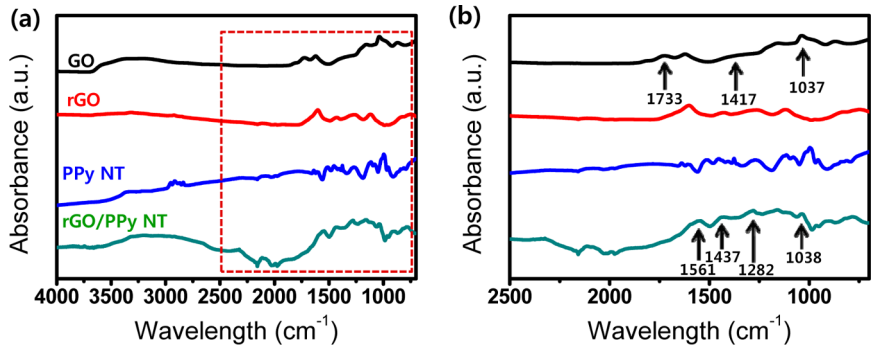

Figure 3. ATR-FT-IR spectra of (a) GO, rGO, PPy, NT, and rGO/PPy NTs composites. A magnified view of the marked area in part a is shown in part b.

NTs and rGO in isolation due to interactions between the rGO layers and PPy NTs.

The XRD diffractograms of GO contained a very sharp peak at 10.1° (d = 8.75 Å), which indicates that the structure of the original graphite was successfully oxidized to GO, as shown in Figure 4. A broad peak appeared at 25° (d = 3.56 Å), which

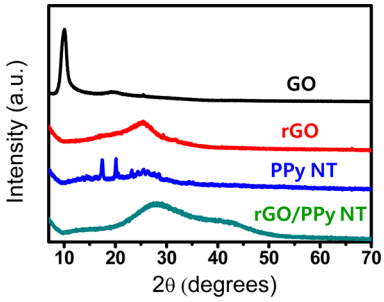

Figure 4. X-ray diffractions of GO, rGO, PPy NT, and rGO/PPy NTs composites.

implies that rGO formation was achieved by reduction of GO using hydrazine. The rGO/PPy NT composites exhibited a broad peak at around 28° (d = 3.18 Å), which corresponds to the pyrrole intermolecular distance between the rGO/PPy NTs. We conclude that the PPy NTs and the rGO sheet formed a composite via $\pi-\pi$ interactions.

The electrical properties of the rGO/PPy NT composites on the patterned electrode substrate were characterized by measuring current−voltage ($I-V$) curves. As shown in Figure 5a, linear $I-V$ curves were observed over a range of −0.4 V to +0.4 V, indicating that Ohmic contacts were formed between the nanocomposites and the gold electrodes. The conductivity of the rGO/PPy NT composites was higher than that of rGO and PPy NTs. It follows that the rGO/PPy NT composites exhibited effective electron transport between the PPy NTs and the rGO, which resulted in a decrease in the resistance. Although the rGO sheet displayed excellent electrical properties, the conductivity was highly anisotropic and interlayer electron transport was slow, as shown in Figure 4a. However, the PPy NTs act as conductive channels to connect the rGO layers, resulting in enhanced conductivity, as shown in Figure 5a.

To investigate the electrical characteristics of the rGO/PPy NT conductive channels, we measured the source-drain current−voltage ($I_{SD}-V_{SD}$) characteristics of liquid-ion-gated transistors under various gate biases. For these measurements, V_g was varied in the range of −2.0 V to +0.4 V in steps of 0.2 V,

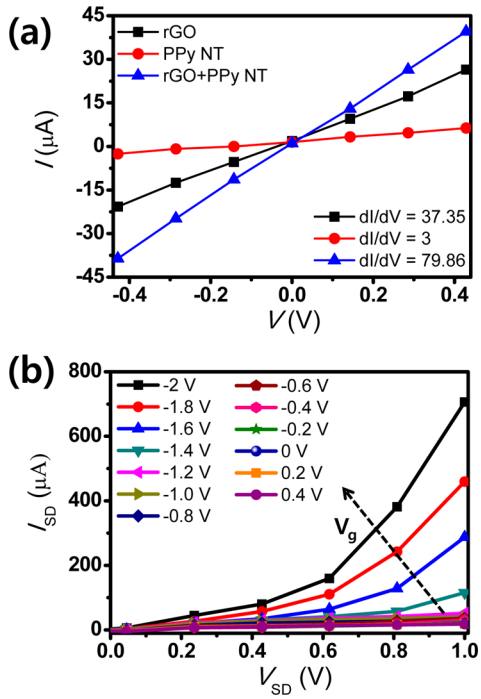

Figure 5. (a) Current−voltage ($I-V$) curves of GO, rGO, PPy NTs, and rGO/PPy NTs composites and (b) rGO/PPy NTs composites at V_g from −2.0 to 0.4 V in 0.2-V steps (V_{sd}: 0 to 1.0 V in 0.2-V steps).

with a gate voltage sweep rate of 0.2 V s^{-1}; the devices were in a phosphate-buffered saline (PBS) solution (pH 7.4), as shown in Figure 5b. I_{SD} increased (i.e., became more positive) when a larger negative gate bias was applied. This is a typical characteristic of p-channel transistors and therefore we conclude that the current in the device was due to hole transport and that the modulation of I_{SD} resulted from control over the hole carrier density at the surface of rGO/PPy NT composites. The p-type semiconductor behavior of PPy materials is well-known.[17] While unaltered graphene exhibits ambipolar properties in electrical devices, the graphene samples used herein exhibited hole-transporting behavior due to the absorption of oxygen and/or water from air[14] to yield rGO/PPy NT composites that behave as enhanced p-type systems. This in turn resulted in higher stability and improved sensing performance relative to that of the individual components alone.

We fabricated liquid-ion-gated FETs, which were surrounded with PBS at pH 7.4 as the electrolyte, as shown in Figure 6a. A

dx.doi.org/10.1021/ac403770x | Anal. Chem. 2014, 86, 1822−1828

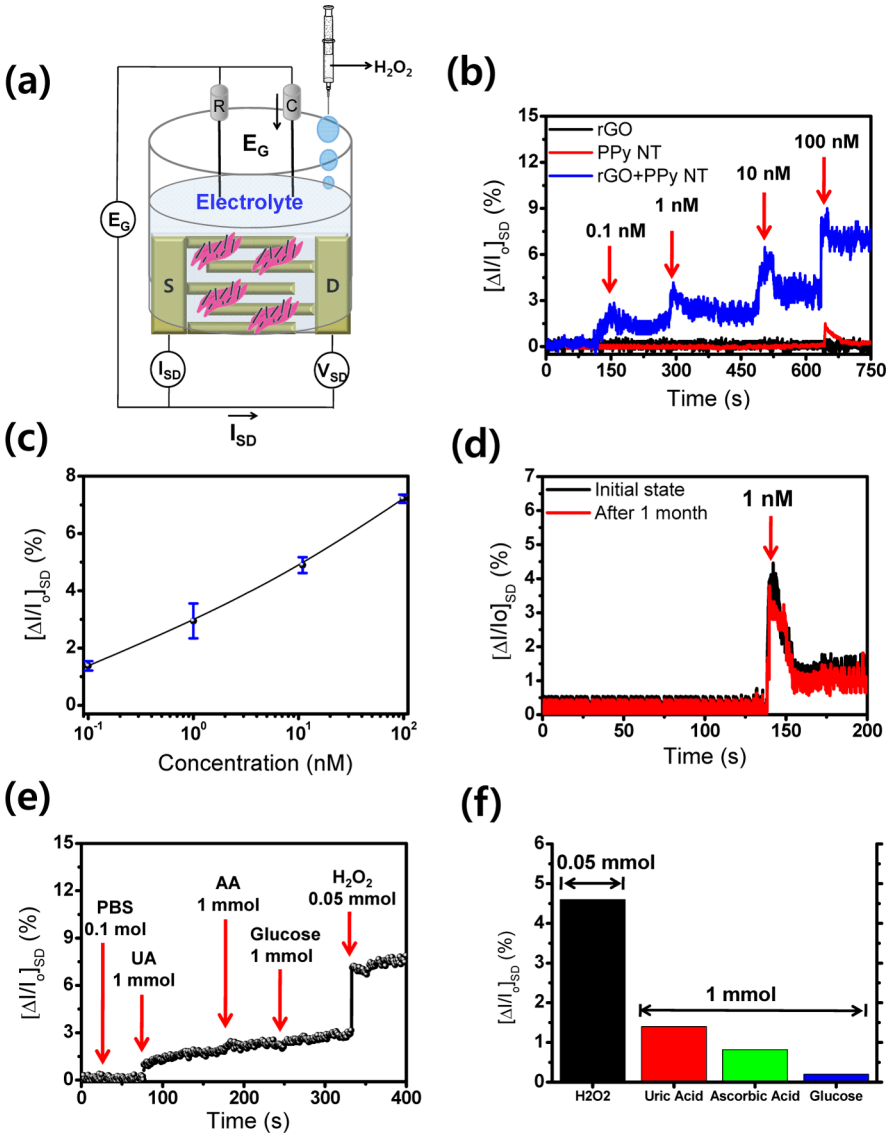

Figure 6. (a) Schematic diagram shows a liquid-ion-gated FET-type sensor based on rGO/PPy NTs. (Ag/AgCl reference electrode, R; platinum counter electrode, C; source and drain electrodes, S and D). (b) Real-time responses and (c) a calibration curve for H_2O_2 based on rGO, PPy NTs, and rGO/PPy NTs composites were measured at V_{sd} = 10 mV (V_g = 0.1 V) with H_2O_2 concentrations of 0.1 nM to 100 nM. Storage stability based on rGO/PPy NT nanohybrid sensor performance is shown in part d. Real-time responses to PBS, UA, AA, glucose, and H_2O_2 are shown in part e. (f) A histogram details the sensing performance of the rGO/PPy NTs composites to UA, AA, glucose, and H_2O_2.

remote electrode in the surrounding electrolyte provided good contact between the rGO/PPy NT composites and the solution. This strategy can enhance the sensing performance of resistive sensors via signal amplification. Using the FET-type sensor as a p-channel FET (with V_g = 0.1 V), we characterized the real-time response to H_2O_2 in varying concentrations. As shown in Figure 6b, the changes in I_{SD} were measured in response to the variation of the H_2O_2 concentration in the solution. The sensitivity was determined from the normalized change in the current $\Delta I_{SD}/I_0 = (I_{SD} - I_0)/I_0$, where I_0 is the initial current and I_{SD} is the measured real-time current following stabilization after changing the H_2O_2 concentration. The sensor exhibited an increase in I_{SD} in response to a gradual increase in the concentration of H_2O_2, which occurred because of the accumulation of p-type charge carriers at the surface of the rGO/PPy NTs composite. (See below for a discussion of the sensor mechanism.) The rGO/PPy NT composites exhibited very sensitive responses to H_2O_2, with a detection limit of approximately 100 pM (signal-to-noise ratio = 3.5). It is generally considered a significant signal when the S/N is greater than or equal to 3.0.[8,9] The S/N (= 0.83) value is too low on the measurement for 10 pM, which means that it is not considered the signal as shown in Figure S1 in the Supporting Information. Thus, 100 pM is a limitation of detection. The response of the FET-type sensor to changes in H_2O_2 concentration was almost instant, enabling far more rapid detection and 10 times better sensitivity compared with oxidation-level-based methods in glassy carbon electrodes (GCEs), as shown in Table 1. Figure 6c shows the calibration curve; stronger signals were detected when the H_2O_2 concentration increased. In all measurements, the FET sensors had rapid response times of less than 1 s and showed linear responses to current changes. The reproducibility and storage stability of the hybrid FET sensors were also evaluated. The response of the H_2O_2 sensor did not change appreciably after 10 repeated experiments, indicating good reproducibility.

dx.doi.org/10.1021/ac403770x | *Anal. Chem.* 2014, 86, 1822−1828

Table 1. Comparison of the Performance of Various H_2O_2 Sensors[a]

biosensor configuration	detection limit (μM)	ref
AgNP/SnO_2/GCE	5	19
AgNP/graphene/GCE	28	20
AgNP/CNT/GCE	0.5	21
AgNP/ZnO/GCE	0.42	22
AgNP/DNA/GCE	1.7	23
AgNP/MWCNT/Au electrode	0.5	24
MnO_2/GO/GCE	0.8	25
Ni/Al-LDHs films	0.009	26
Co/Al-LDHs films	0.05	26
Pt/PPy Hollow microsphere	1	27
Pt/graphene/GCE	0.5	28
Fe_3O_4/rGO/GCE	0.006	29
PPy NWs/Cu/Au electrode	2.3	30
Hb/CeO_2/MWNTs	0.65	31
PPy NT/rGO FET-type sensor	0.0001	this work

[a]NP = nanoparticle, NW = nanowire, rGO = reduced graphene oxide, GCE = glassy carbon electrode, MWCNT = multiwall carbon nanotube, Hb = hemoglobin, LDH = layered double hydroxides.

Storage stability was assessed in air. After 1 month of storage, the FET sensor detected 1 nM of H_2O_2, as shown in Figure 6d, with no change in the response current relative to that of freshly prepared sensors. This indicates excellent air and storage stability.

To understand the mechanism of H_2O_2 sensing, we monitored the real-time response of the FET-type sensor based on PPy NTs as well as sensors based on rGO materials, both at V_g = 0.1 V. The sensor device based on PPy NTs was sensitive to H_2O_2 at a concentration of 1 μM, as shown in Figure 6b. The sensing device based on an rGO layer was sensitive to H_2O_2 at a concentration of 1 mM. This shows that H_2O_2 can alter the electrical signal more efficiently in PPy NTs than in rGO. The applied gate bias of V_g = 0.1 V was less than the oxidation potential of H_2O_2, which means the modulation of I_{SD} did not occur because of electrochemical oxidation of H_2O_2. Therefore, H_2O_2 was able to change the charge carrier density more effectively in the PPy backbone than in the graphene backbone by reacting with PPy to produce a positive charge. It has been reported that p-doping effects result from the addition of H_2O_2 molecules as opposed to the direct transfer of electrons via oxidative reactions between the graphene and PPy backbone.[18] The reasons for the enhanced performance of the sensor based on the rGO/PPy NT composites are due to the following effects. First, an efficient response to H_2O_2 occurred due to the enhanced surface area and strong interactions between the rGO sheet and PPy NTs. Second, the enhanced p-type semiconductor behavior improved signal transduction.

The specificity of the response to H_2O_2 was evaluated by real-time monitoring of I_{SD} in various solutions containing compounds found in biological fluids, including UA, AA, and glucose solutions (see Figure 6e). The real-time responses were detected in response to injecting 1-mM UA, 1-mM AA, 1-mM glucose, and 0.05-mM H_2O_2. A remarkable increase in the current occurred when H_2O_2 was injected, even at far lower concentrations than the other compounds in the analyte, as shown in Figure 6f. Exposure of the sensors to UA and AA did not significantly change the charge density on the surface of the rGO/PPy NTs relative to the changes observed upon exposure to H_2O_2. Glucose was not able to bind to the graphene-PPy nanohybrid materials due to the lack of an appropriate binding site. These results clearly demonstrate specificity toward H_2O_2.

CONCLUSIONS

We demonstrated high sensitivity and specificity toward H_2O_2 using a liquid-ion-gated FET sensor based on rGO/PPy nanocomposites. We characterized the composite material using Raman and ATR-FT-IR spectroscopy. The fabricated FET devices exhibited p-channel behavior, with good electrical conductivity, and Ohmic contacts were formed with the source and drain electrodes. The FET-type sensor system described herein exhibited a rapid response to changes in H_2O_2 concentration with a detection limit of 100 pM. These results are more favorable than those in previous reports describing biosensors for H_2O_2. The current biosensor was highly reproducible and stable in air. We also demonstrated specificity toward H_2O_2 by characterizing the response of the biosensor in solutions containing UA, AA, and glucose. From the perspective of sensor performance, these FET-type biosensors based on rGO/PPy NTs can be used in food and environmental applications as alternative methods for the detection of H_2O_2.

ASSOCIATED CONTENT

Supporting Information

Additional information as noted in text. This material is available free of charge via the Internet at http://pubs.acs.org.

AUTHOR INFORMATION

Corresponding Author

*E-mail: jsjang@plaza.snu.ac.kr. Fax: (+82) 2-888-1604.

Notes

The authors declare no competing financial interest.

ACKNOWLEDGMENTS

This research was supported by the National Research Foundation of Korea (NRF) grant funded by the Korean government (MEST) (Grant No. 2011-0017125)

REFERENCES

(1) (a) Vione, D.; Maurino, V.; Minero, C.; Borghesi, D.; Lucchiari, M.; Pelizzetti, E. *Environ. Sci. Technol.* **2003**, *37*, 4635−4641. (b) Shu, X.; Chen, Y.; Yuan, H.; Gao, S.; Xiao, D. *Anal. Chem.* **2007**, *79*, 3695−3702. (c) Wang, Y.; Huang, J.; Zhang, C.; Wei, J.; Zhou, X. *Electroanalysis* **1998**, *10*, 776−778. (d) Gilpin, R. K.; Pachla, L. A. *Anal. Chem.* **2005**, *77*, 3755−3770.

(2) (a) Ohshima, H.; Tatemichi, M.; Sawa, T. *Arch. Biochem. Biophys.* **2003**, *417*, 3−11. (b) Maruyama, W.; Dostert, P.; Matsubara, K.; Naoi, M. *Free Radical Biol. Med.* **1995**, *19*, 67−75. (c) Amatore, C.; Arbault, S.; Bruce, D.; de Oliveira, P.; Erard, M.; Vuillaume, M. *Chem.−Eur. J.* **2001**, *7*, 4171−4179.

(3) (a) Foreman, J.; Demidchik, V.; Bothwell, J. H. F.; Mylona, P.; Miedema, H.; Torres, M. A.; Linstead, P.; Costa, S.; Brownlee, C.; Jones, J. D. G.; Davies, J. M.; Dolan, L. *Nature* **2003**, *422*, 442−446. (b) Lambeth, J. D. *Nat. Rev. Immunol.* **2004**, *4*, 181−189. (c) Niethammer, P.; Grabher, C.; Look, A. T.; Mitchison, T. J. *Nature* **2009**, *459*, 996−999. (d) Sauer, H.; Rahimi, G.; Hescheler, J.; Wartenberg, M. *FEBS Lett.* **2000**, *476*, 218−223.

(4) (a) Sunil, K.; Narayana, B. *Bull. Environ. Contam. Toxicol.* **2008**, *81*, 422−426. (b) Xu, S.; Peng, B.; Han, X. *Biosens. Bioelectron.* **2007**, *22*, 1807−1810. (c) Song, Y.; Wei, W.; Qu, X. *Adv. Mater.* **2011**, *23*, 4215−4236. (d) Wang, K.; Liu, Q.; Wu, X.-Y.; Guan, Q.-M.; Li, H.-N. *Talanta* **2010**, *82*, 372−376.

(5) (a) Bai, J.; Jiang, X. *Anal. Chem.* **2013**, *85*, 8095−8101. (b) Kafi, A. K. M.; Ahmadalinezhad, A.; Wang, J.; Thomas, D. F.; Chen, A. *Biosens. Bioelectron.* **2010**, *25*, 2458−2463. (c) Sun, X.; Guo, S.; Liu, Y.; Sun, S. *Nano Lett.* **2012**, *12*, 4859−4863. (d) Wang, Y.; Yang, X.; Bai, J.; Jiang, X.; Fan, G. *Biosens. Bioelectron.* **2013**, *43*, 180−185.
(6) (a) Kwon, O. S.; Lee, S. H.; Park, S. J.; An, J. H.; Song, H. S.; Kim, T.; Oh, J. H.; Bae, J.; Yoon, H.; Park, T. H.; Jang, J. *Adv. Mater.* **2013**, *25*, 4177−4185. (b) Park, S. J.; Kwon, O. S.; Lee, S. H.; Song, H. S.; Park, T. H.; Jang, J. *Nano Lett.* **2012**, *12*, 5082−5090.
(7) (a) Yoon, H.; Lee, S. H.; Kwon, O. S.; Song, H. S.; Oh, E. H.; Park, T. H.; Jang, J. *Angew. Chem., Int. Ed.* **2009**, *48*, 2755−2758. (b) Schierhorn, M.; Boettcher, S. W.; Kraemer, S.; Stucky, G. D.; Moskovits, M. *Nano Lett.* **2009**, *9*, 3262−3267. (c) Lee, J. I.; Cho, S. H.; Park, S.-M.; Kim, J. K.; Kim, J. K.; Yu, J.-W.; Kim, Y. C.; Russell, T. P. *Nano Lett.* **2008**, *8*, 2315−2320. (d) Potyrailo, R. A. *Angew. Chem., Int. Ed.* **2006**, *45*, 702−723.
(8) Kwon, O. S.; Park, S. J.; Jang, J. *Biomaterials* **2010**, *31*, 4740−4747.
(9) Yoon, H.; Ko, S.; Jang, J. *J. Phys. Chem. B* **2008**, *112*, 9992−9997.
(10) (a) Geim, A. K. *Science* **2009**, *324*, 1530−1534. (b) Geim, A. K.; Novoselov, K. S. *Nat. Mater.* **2007**, *6*, 183−191.
(11) (a) Balandin, A. A.; Ghosh, S.; Bao, W.; Calizo, I.; Teweldebrhan, D.; Miao, F.; Lau, C. N. *Nano Lett.* **2008**, *8*, 902−907. (b) Kim, K. S.; Zhao, Y.; Jang, H.; Lee, S. Y.; Kim, J. M.; Kim, K. S.; Ahn, J.-H.; Kim, P.; Choi, J.-Y.; Hong, B. H. *Nature* **2009**, *457*, 706−710. (c) Zhang, Y.; Tan, Y.-W.; Stormer, H. L.; Kim, P. *Nature* **2005**, *438*, 201−204.
(12) Kwak, Y. H.; Choi, D. S.; Kim, Y. N.; Kim, H.; Yoon, D. H.; Ahn, S.-S.; Yang, J.-W.; Yang, W. S.; Seo, S. *Biosens. Bioelectron.* **2012**, *37*, 82−87.
(13) (a) Kamat, P. V. *J. Phys. Chem. Lett.* **2009**, *1*, 520−527. (b) Li, D.; Kaner, R. B. *Science* **2008**, *320*, 1170−1171. (c) Xu, C.; Wang, X.; Zhu, J. *J. Phys. Chem. C* **2008**, *112*, 19841−19845.
(14) (a) Shin, K.-Y.; Hong, J.-Y.; Jang, J. *Adv. Mater.* **2011**, *23*, 2113−2118. (b) Sun, Z.; Yan, Z.; Yao, J.; Beitler, E.; Zhu, Y.; Tour, J. M. *Nature* **2010**, *468*, 549−552. (c) Yang, W.; Ratinac, K. R.; Ringer, S. P.; Thordarson, P.; Gooding, J. J.; Braet, F. *Angew. Chem., Int. Ed.* **2010**, *49*, 2114−2138.
(15) (a) Yang, X.; Zhu, Z.; Dai, T.; Lu, Y. *Macromol. Rapid Commun.* **2005**, *26*, 1736−1740. (b) Tingyang, D.; Xiaoming, Y.; Yun, L. *Nanotechnology* **2006**, *17*, 3028.
(16) Hummers, W. S.; Offeman, R. E. *J. Am. Chem. Soc.* **1958**, *80*, 1339−1339.
(17) Kwon, O. S.; Ahn, S. R.; Park, S. J.; Song, H. S.; Lee, S. H.; Lee, J. S.; Hong, J.-Y.; Lee, J. S.; You, S. A.; Yoon, H.; Park, T. H.; Jang, J. *ACS Nano* **2012**, *6*, 5549−5558.
(18) Huang, Y.; Dong, X.; Shi, Y.; Li, C. M.; Li, L.-J.; Chen, P. *Nanoscale* **2010**, *2*, 1485−1488.
(19) Miao, Y.-E.; He, S.; Zhong, Y.; Yang, Z.; Tjiu, W. W.; Liu, T. *Electrochim. Acta* **2013**, *99*, 117−123.
(20) Liu, S.; Tian, J.; Wang, L.; Li, H.; Zhang, Y.; Sun, X. *Macromolecules* **2010**, *43*, 10078−10083.
(21) Zhao, W.; Wang, H.; Qin, X.; Wang, X.; Zhao, Z.; Miao, Z.; Chen, L.; Shan, M.; Fang, Y.; Chen, Q. *Talanta* **2009**, *80*, 1029−1033.
(22) Wang, Q.; Zheng, J. *Microchim. Acta* **2010**, *169*, 361−365.
(23) Cui, K.; Song, Y.; Yao, Y.; Huang, Z.; Wang, L. *Electrochem. Commun.* **2008**, *10*, 663−667.
(24) Zhao, W.; Wang, H.; Qin, X.; Wang, X.; Zhao, Z.; Miao, Z.; Chen, L.; Shan, M.; Fang, Y.; Chen, Q. *Talanta* **2009**, *80*, 1029−1033.
(25) Li, L.; Du, Z.; Liu, S.; Hao, Q.; Wang, Y.; Li, Q.; Wang, T. *Talanta* **2010**, *82*, 1637−1641.
(26) Yin, Z.; Wu, J.; Yang, Z. *Biosens. Bioelectron.* **2011**, *26*, 1970−1974.
(27) Li, Y.; Chang, Y.; Jin, M.; Liu, Y.; Han, G. *J. Appl. Polym. Sci.* **2012**, *126*, 1316−1321.
(28) Xu, F.; Sun, Y.; Zhang, Y.; Shi, Y.; Wen, Z.; Li, Z. *Electrochem. Commun.* **2011**, *13*, 1131−1134.
(29) Teymourian, H.; Salimi, A.; Khezrian, S. *Biosens. Bioelectron.* **2013**, *49*, 1−8.
(30) Zhang, T.; Yuan, R.; Chai, Y.; Li, W.; Ling, S. *Sensors* **2008**, *8*, 5141−5152.
(31) Zhang, X.; Qi, B.; Zhang, S. *Anal. Lett.* **2008**, *41*, 3100−3112.